Journal Pre-proof

A semi-discrete line-free method of monopoles for dislocation dynamics

M.P. Ariza, M. Ortiz

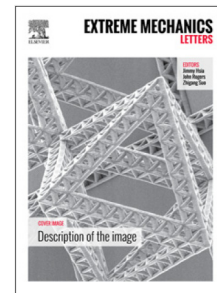Please cite this article as: M.P. Ariza and M. Ortiz, A semi-discrete line-free method of monopoles for dislocation dynamics, *Extreme Mechanics Letters* (2021), doi: https://doi.org/10.1016/j.eml.2021.101267.

This is a PDF file of an article that has undergone enhancements after acceptance, such as the addition of a cover page and metadata, and formatting for readability, but it is not yet the definitive version of record. This version will undergo additional copyediting, typesetting and review before it is published in its final form, but we are providing this version to give early visibility of the article. Please note that, during the production process, errors may be discovered which could affect the content, and all legal disclaimers that apply to the journal pertain.

A semi-discrete line-free method of monopoles for dislocation dynamics

M. P. Ariza[a], M. Ortiz[b,*]

[a]*Escuela Técnica Superior de Ingeniería, University of Seville, 41092 Seville, Spain*
[b]*Division of Engineering and Applied Science, California Institute of Technology, 1200 E. California Blvd., Pasadena, CA 91125.*

Abstract

We develop a semi-discrete particle method for Volterra dislocation currents in which the particles, or monopoles, represent an element of line and carry a Burgers vector. The monopoles move according to mobility kinetics driven by elastic and applied forces. The divergence constraint of Volterra dislocation currents is enforced weakly through mesh-free interpolation and an explicit linear connectivity, or 'sequence', between the monopoles need not be defined. In this sense, the method is 'line-free', i. e., it sidesteps the need to track dislocation lines. This attribute offers significant computational advantages in terms of simplicity, robustness and efficiency, especially as regards the tracking of complex dislocation patterns, including topological transitions. We illustrate the range and scope of the method, by means of an example of application concerned with the plastic hardening of nano-sized grains under monotonic loading.

Keywords: Dislocation dynamics, Dislocation transport, Discrete dislocations, Method of monopoles, Particle methods

1. Introduction

Particle methods have attained considerable acceptance for the discretization and numerical solution of transport problems. For the most part, particle methods have been developed for scalar densities such as mass, concentration and heat [1, 2]. In this setting, particles maybe regarded as Dirac-delta approximations of otherwise continuous measures, or densities. However, there are many transport problems of interest where the measure being transported is concentrated on lines or surfaces and may carry a vector 'charge'. Such measures are often closed, i. e., have no boundary and, therefore, satisfy divergence or curl constraints. A case in point concerns Volterra dislocations, whose Nye measure is concentrated on lines

that carry a conserved vector charge, the Burgers vector. These types of measures are collectively referred to as *currents*. In contrast to scalar measures, particle methods for general currents is comparatively much less developed.

Deffo *et al.* [3] have developed a particle method for Volterra dislocation currents in which the particles, or monopoles, represent an element of line and carry a Burgers vector. The monopoles move according to mobility kinetics driven by elastic and applied forces. The divergence constraint of Volterra dislocation currents is enforced weakly through mesh-free interpolation. The fundamental difference with traditional approximation schemes based on segments is that an explicit linear connectivity, or 'sequence', between the monopoles need not be defined. Instead, the monopoles move as an unstructured system of particles subject to the weak divergence constraint. In this sense, the method is 'line-free', i. e., it sidesteps the need to track dislocation lines. This

*Corresponding author
Email address: ortiz@caltech.edu (M. Ortiz)

attribute offers significant computational advantages in terms of simplicity, robustness and efficiency, especially as regards the tracking of complex dislocation patterns, including topological transitions.

The formulation of Deffo *et al.* [3] is fully discrete, in the sense that both space and time are jointly discretized. In addition, time discretization is effected using optimal transport tools such as the Wasserstein distance. In the present work, we reformulate the method is semi-discrete form, i. e., we discretize the dislocation transport problem in space but not in time. By keeping time continuous, the resulting semi-discrete theory is analytically simple and reveals more clearly the structure of the monopole discretization. In addition, the semi-discrete formulation lends itself to the application of general time integration schemes, explicit and implicit. We illustrate these trade-offs, and the range and scope of the method, by means of an example of application concerned with the plastic hardening of nano-sized grains under monotonic loading.

2. Volterra dislocations

2.1. The Nye dislocation density

We specifically consider a distribution of Volterra dislocations, characterized by a collection of oriented dislocation lines described locally by parametric equations $\boldsymbol{x}(s)$ in terms of a local parameter s, not necessarily the arc-length, and carrying a local Burgers vector $\boldsymbol{b}(s)$. A rigorous mathematical treatment of dislocation densities as *currents* may be found in [4, 5]. To every element of dislocation line we can associate a differential of *Nye dislocation density*

$$d\alpha_{ij}(s) = b_i(s)dx_j(s) = b_i(s)t_j(s)\,ds, \quad (1)$$

where

$$t_i(s) = x_i'(s) \quad (2)$$

is tangent to the dislocation line. We note that representation (1) is invariant under reparameterization of the dislocation line. The dislocation line separates regions of constant displacement jump within slip surfaces and, therefore, the Nye dislocation density $\boldsymbol{\alpha}$ is closed or *divergence-free*. This closeness

or divergence-free condition in turn implies that the dislocation line has no boundary, i. e., dislocations cannot terminate in the bulk but must instead form closed loops or networks or exit through the boundary. It also implies Frank's rule for dislocation junctions (cf., e. g., [6]).

2.2. The energy of Volterra dislocations

Formally, the elastic energy of a dislocation density $\boldsymbol{\alpha}$ in a homogeneous infinite solid is

$$E(\boldsymbol{\alpha}) = \min_{\beta} \int W(\boldsymbol{\beta})\,dV, \quad (3a)$$

$$\text{subject to: } \beta_{ik,l}e_{lkj} = \alpha_{ij}, \quad (3b)$$

where $\boldsymbol{\beta}$ is the elastic distortion of the lattice,

$$W(\boldsymbol{\beta}) = \frac{1}{2}c_{ijkl}\beta_{ij}\beta_{kl} \quad (4)$$

is the elastic strain energy, with elastic moduli $c_{ijkl} = c_{klij} = c_{jikl} = c_{ijlk}$, e_{ijk} is the Levi-Civita permutation tensor, dV is the element of volume and the integral extends to the infinite domain of the solid. In areas of the solid free of dislocations, $\boldsymbol{\beta}$ can be identified with the local displacement gradient $\nabla \boldsymbol{u}$.

As is well-known, the elastic energy (3a) diverges logarithmically for Volterra dislocations. In order to eliminate this divergence, proper account needs to be taken of the structure of the dislocation core. A simple core model, and attendant energy regularization thereof, can be formulated by spreading, or mollifying, a Volterra dislocation density $\boldsymbol{\alpha}$ into [3]

$$\boldsymbol{\alpha}^\epsilon(\boldsymbol{x}) = \int \phi^\epsilon(\boldsymbol{x} - \boldsymbol{x}')\,d\boldsymbol{\alpha}(\boldsymbol{x}') \equiv \phi^\epsilon * \boldsymbol{\alpha}(\boldsymbol{x}), \quad (5)$$

where $*$ denotes the convolution operator and

$$\phi^\epsilon(\boldsymbol{x}) = \frac{1}{4\pi\epsilon^2 r}\,e^{-|\boldsymbol{x}|/\epsilon}, \quad (6)$$

is a mollifier that fits the dislocation lines with a core of size ϵ. The regularized energy of a Volterra dislocation density $\boldsymbol{\alpha}$ is, then,

$$E^\epsilon(\boldsymbol{\alpha}) = E(\boldsymbol{\alpha}^\epsilon), \quad (7)$$

with $E(\boldsymbol{\alpha}^\epsilon)$ given by (3a). We note that $E^\epsilon(\boldsymbol{\alpha})$ is now finite since $E(\boldsymbol{\alpha}^\epsilon)$ is evaluated for a dislocation

2

density $\boldsymbol{\alpha}^\epsilon$ with a finite core size ϵ. A derivation of this core regularization from strain-gradient elasticity may be found in [3]. For isotropic linear elasticity, the energy (7) specializes to [6, 3]

$$
\begin{aligned}
E^\epsilon(\boldsymbol{\alpha}) = \\
- \frac{\mu}{4\pi} \int_\Gamma \int_\Gamma S^{\epsilon\epsilon} (\boldsymbol{b} \times \boldsymbol{b}') \cdot (\boldsymbol{t} \times \boldsymbol{t}') \, ds \, ds' \\
+ \frac{\mu}{8\pi} \int_\Gamma \int_\Gamma S^{\epsilon\epsilon} (\boldsymbol{b} \cdot \boldsymbol{t})(\boldsymbol{b}' \cdot \boldsymbol{t}') \, ds \, ds' + \\
\frac{\mu}{8\pi(1 - \nu)} \int_\Gamma \int_\Gamma (\boldsymbol{b} \times \boldsymbol{t}) \cdot \boldsymbol{T}^{\epsilon\epsilon} \cdot (\boldsymbol{b}' \times \boldsymbol{t}') \, ds \, ds',
\end{aligned}
\tag{8}
$$

where μ is the shear modulus, ν Poisson's ratio,

$$
S^{\epsilon\epsilon}(\boldsymbol{x}, \boldsymbol{x}') = \frac{2\epsilon - (r + 2\epsilon)\mathrm{e}^{-r/\epsilon}}{2\epsilon r}, \tag{9a}
$$

$$
R^{\epsilon\epsilon}(\boldsymbol{x}, \boldsymbol{x}') = \frac{r^2 + 4\epsilon^2 - \epsilon(r + 4\epsilon)\mathrm{e}^{-r/\epsilon}}{r}, \tag{9b}
$$

$$
T_{ij}^{\epsilon\epsilon}(\boldsymbol{x}, \boldsymbol{x}') = \frac{\partial^2 R^{\epsilon\epsilon}}{\partial x_i \partial x_j'}, \tag{9c}
$$

and $r = |\boldsymbol{x} - \boldsymbol{x}'|$.

2.3. Dislocation transport

Next we consider a collection of moving Volterra dislocation lines described by parametric equations $\boldsymbol{x}(s, t)$ and carrying a local Burgers vector $\boldsymbol{b}(s, t)$, where s is a fixed local parameter, e. g., the arc-length measured over a reference configuration of the dislocation line, and t denotes time. Moving dislocations satisfy the transport equation (cf. [7], eqs. (32.2) and (38.4))

$$
\dot{\alpha}_{ij} - e_{jlk} e_{mnk} (v_m \alpha_{in})_{,l} = 0, \tag{10}
$$

where $\boldsymbol{v}(s, t)$ is the dislocation velocity. We note that, in view of the representation (1), only the component of $\boldsymbol{v}(s, t)$ perpendicular to the dislocation line has an effect on the dislocation density, as expected. We also note that, for Volterra dislocations concentrated on lines, eq. (10) needs to be understood distributionally, or in a weighted sense. Formally taking the divergence of the transport equation (10) gives

$$
\dot{\alpha}_{ij,j} = e_{jlk} e_{mnk} (v_m \alpha_{in})_{,lj} = 0, \tag{11}
$$

which shows that dislocation transport is divergence-preserving. In particular, if the dislocation density is divergence-free initially, it subsequently remains so for all time. Differentiating (2) with respect to time, we obtain the identity

$$
\dot{t}_i(s, t) = v_i'(s, t), \tag{12}
$$

which governs the local reorientation and stretching of the dislocation line. The identity sets forth a non-holonomic kinematic constraint that ties the rate of change of the elements of line $\boldsymbol{t}(s, t)$, including stretching and reorientation, to the velocity $\boldsymbol{v}(s, t)$ of the dislocation line. It is also readily verified [3], using representation (2), that, for continuous evolutions in the absence of topological transitions, the kinematic constraint (12) is locally equivalent the transport equation (10) provided that, in addition,

$$
\dot{b}_i(s, t) = 0, \tag{13}
$$

which is a statement of conservation of Burgers vector.

2.4. Configurational forces

A classical calculation shows that the Peach-Köhler force is the configurational driving force for $\boldsymbol{v}(s, t)$. The standard derivation may be adapted to account for the core regularization (5). To this end, we begin by enforcing the constraint (3b) by means of Lagrange multipliers, leading to the Lagrangian

$$
\begin{aligned}
L^\epsilon(\beta, \chi; \alpha) = \\
\int \Big(W(\boldsymbol{\beta}) + \chi_{ij}(\beta_{ik,l} e_{lkj} - \alpha_{ij}^\epsilon) \Big) \, dV.
\end{aligned}
\tag{14}
$$

The corresponding stationarity equations are

$$
\sigma_{ik}^\epsilon = \chi_{ij,l}^\epsilon e_{lkj}, \tag{15a}
$$

$$
\alpha_{ij}^\epsilon = \beta_{ik,l}^\epsilon e_{lkj}, \tag{15b}
$$

where $\boldsymbol{\beta}^\epsilon$ and $\boldsymbol{\chi}^\epsilon$ are the elastic distortion and Lagrange multiplier at equilibrium, and

$$
\sigma_{ik}^\epsilon = \frac{\partial W}{\partial \beta_{ik}}(\boldsymbol{\beta}^\epsilon) = c_{ikjl} \beta_{jl}^\epsilon \tag{16}
$$

3

is the stress field at equilibrium. We note that (15a) identifies $\boldsymbol{\chi}^\epsilon$ as the Airy stress function. Taking rates in (3a) and using (3b) and (15) further gives

$$\dot{E}^\epsilon = \int \sigma_{ik}^\epsilon \dot{\beta}_{ik}^\epsilon \, dV = \int \chi_{ij}^\epsilon \, d\dot{\alpha}_{ij}^\epsilon, \qquad (17)$$

which shows that the Airy stress function $\boldsymbol{\chi}^\epsilon$ is the configurational force driving the dislocation density $\boldsymbol{\alpha}^\epsilon$. Further inserting the transport equation (10) into (17) and using (15a), we obtain

$$\dot{E}^\epsilon = \int \chi_{ij}^\epsilon d\dot{\alpha}_{ij} = \int \chi_{ij}^\epsilon (\phi^\epsilon * d\dot{\alpha}_{ij}) =$$

$$\int (\phi^\epsilon * \chi_{ij}^\epsilon) \, d\dot{\alpha}_{ij} = \int (\phi^\epsilon * \chi_{ij}^\epsilon)_{,l} \, e_{jlk} e_{mnk} v_m \, d\alpha_{in} =$$

$$\int (\phi^\epsilon * \sigma_{ik}^\epsilon) e_{mnk} v_m \, d\alpha_{in} = \int \sigma_{ik}^{\epsilon\epsilon} e_{nmk} v_m \, d\alpha_{in} =$$

$$\int_\Gamma \sigma_{ik}^{\epsilon\epsilon} e_{nmk} v_m b_i t_n \, ds = \int_\Gamma f_m^{\epsilon\epsilon} v_m \, ds, \qquad (18)$$

where

$$\sigma_{ik}^{\epsilon\epsilon} = \phi^\epsilon * \sigma_{ik}^\epsilon = \phi^\epsilon * \phi^\epsilon * \sigma_{ik} \qquad (19)$$

and

$$f_m^{\epsilon\epsilon} = \sigma_{ik}^{\epsilon\epsilon} e_{nmk} b_i t_n \qquad (20)$$

are a twice-regularized equilibrium stress and Peach-Köhler force per unit dislocation length.

2.5. Dislocation mobility

Assuming Onsager kinetics, the dislocation motion is then governed by a mobility law of the type

$$v_i = D_i \psi^*(\boldsymbol{f}^{\epsilon\epsilon}), \qquad (21)$$

where $\psi^*(\boldsymbol{f})$ is a dual kinetic potential and D_i denotes partial differentiation. Alternatively, we may express the mobility law in inverse form as

$$f_i^{\epsilon\epsilon} = D_i \psi(\boldsymbol{v}), \qquad (22)$$

where the kinetic potential $\psi(\boldsymbol{v})$ is the Legendre transform of $\psi^*(\boldsymbol{f})$. A simple example of kinetics is supplied by a linear mobility law, in which case

$$\psi^*(\boldsymbol{f}^{\epsilon\epsilon}) = \frac{M}{2} |\boldsymbol{f}^{\epsilon\epsilon}|^2, \qquad (23)$$

where M is the dislocation mobility. For instance, if the rate-limiting mechanism is phonon drag, then $M = 1/B$, where B the phonon drag coefficient [6].

2.6. Rate problem

Eq. (26), together with (20) define a *rate problem* for the dislocation velocity $\boldsymbol{v}(s,t)$ at time t, given the dislocation geometry $\boldsymbol{x}(s,t)$ at the same time. The rate problem can be expressed variationally by means of the energy-dissipation functional

$$F^\epsilon(\boldsymbol{v}(t); \boldsymbol{x}(t)) = \int_\Gamma \psi(\boldsymbol{v}(s,t)) \, ds +$$
$$\int_\Gamma \left(f_m^{\epsilon\epsilon}(s, \boldsymbol{x}(t)) + f_m^{\text{ext}}(s,t) \right) v_m(s,t) \, ds, \qquad (24)$$

to be minimized with respect to $\boldsymbol{v}(s,t)$ at given $\boldsymbol{x}(s,t)$. In writing (24), we denote by $\boldsymbol{x}(t)$ and $\boldsymbol{v}(t)$ the functions $\boldsymbol{x}(\cdot,t)$ and $\boldsymbol{v}(\cdot,t)$ defined over the entire dislocation line Γ. We also allow for an externally applied Peach-Koehler force of the form

$$\boldsymbol{f}^{\text{ext}}(s,t) = \left(\boldsymbol{\sigma}^{\text{ext}}(t) \boldsymbol{b}(s,t) \right) \times \boldsymbol{t}(s,t), \qquad (25)$$

where $\boldsymbol{\sigma}^{\text{ext}}(t)$ is a time-dependent applied stress.

The Euler-Lagrange equations corresponding to the rate-functional (24) follow as

$$f_i^{\epsilon\epsilon}(s, \boldsymbol{x}(t)) + f_i^{\text{ext}}(s,t) = D_i \psi(\boldsymbol{v}(s,t)), \qquad (26)$$

which extends the mobility law (26) to the case of applied stresses. The requirement that eq. (26) hold for all times defines an evolution problem for the dislocation geometry $\boldsymbol{x}(t)$.

3. Monopole discretization

A natural and computationally convenient spatial discretization of the dislocation measure is as a linear combination of *dislocation monopoles* [3], i. e.,

$$\boldsymbol{\alpha}(t) = \sum_{a=1}^M \boldsymbol{b}_a(t) \otimes \boldsymbol{\xi}_a(t) \, \delta_{\boldsymbol{x}_a(t)}, \qquad (27)$$

where $\boldsymbol{x}_a(t)$ is the position of monopole a at time t, $\boldsymbol{b}_a(t)$ its Burgers vector, $\boldsymbol{\xi}_a(t)$ its element of line, $\delta_{\boldsymbol{x}_a(t)}$ is the Dirac-delta distribution centered at $\boldsymbol{x}_a(t)$, and M is the number of dislocation monopoles, cf. Fig. 1. We may regard each monopole as a particle carrying a dyad composed of a Burgers vector and an element of line. It bears emphasis that the *ansatz* (27) represents an *unstructured* monopole ensemble. In particular, no connectivity or sequencing between the monopoles is implied by the representation.
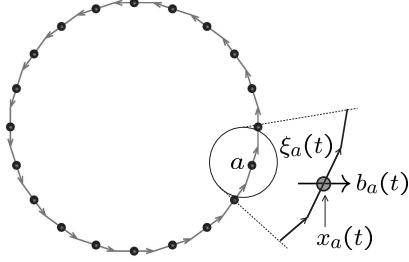
4

Figure 1: Discretization of a circular loop into monopoles. Monopole a is located at $\boldsymbol{x}_a(t)$ and carries an element of line $\boldsymbol{\xi}_a(t)$ and a Burgers vector $\boldsymbol{b}_a(t)$.

3.1. Discrete transport equations

For the monopole ensemble, the discrete counterpart of the transport equations (12) and (13) is

$$\dot{\boldsymbol{b}}_a(t) = \boldsymbol{0}, \tag{28a}$$

$$\dot{\boldsymbol{\xi}}_a(t) = \nabla \boldsymbol{v}_a(t) \boldsymbol{\xi}_a(t), \tag{28b}$$

where

$$\boldsymbol{v}_a(t) = \dot{\boldsymbol{x}}_a(t) \tag{29}$$

is the velocity of monopole a. From these relations, we see that, barring topological transitions, the monopoles carry a constant Burgers vector, eq. (28a), and that the reorientation and stretching of the elements of line is determined by the tangential gradient of the velocity field, eq. (28b). The computation of the latter requires an interpolation scheme of the general form

$$\boldsymbol{v}(\boldsymbol{x}, t) = \sum_{a=1}^{M} \boldsymbol{v}_a(t) N_a(\boldsymbol{x}, t), \tag{30}$$

where $\{N_a, \ 1, \dots, M\}$ are shape functions satisfying the first-order consistency condition

$$\sum_{a=1}^{M} N_a(\boldsymbol{x}, t) = 1. \tag{31}$$

Differentiating (30), we further obtain

$$\nabla \boldsymbol{v}(\boldsymbol{x}, t) = \sum_{a=1}^{M} \boldsymbol{v}_a(t) \otimes \nabla N_a(\boldsymbol{x}, t). \tag{32}$$

Inserting (32) into (28b) gives

$$\dot{\boldsymbol{\xi}}_a(t) = \sum_{b=1}^{M} \left(\nabla N_b(\boldsymbol{x}_a, t) \cdot \boldsymbol{\xi}_a(t) \right) \boldsymbol{v}_b(t), \tag{33}$$

which fully discretizes the kinematic constraint (28b).

In keeping with the objective of a line-free method, we choose a mesh-free scheme for the interpolation (30) of the velocity $\boldsymbol{v}(\boldsymbol{x}, t)$. In calculations we specifically use the max-ent shape functions [8]

$$N_a(\boldsymbol{x}, t) = \frac{1}{Z(\boldsymbol{x}, t)} \exp\left(-\frac{\beta_a}{2} |\boldsymbol{x} - \boldsymbol{x}_a(t)|^2 \right), \tag{34}$$

where

$$Z(\boldsymbol{x}, t) = \sum_{a=1}^{M} \exp\left(-\frac{\beta_a}{2} |\boldsymbol{x} - \boldsymbol{x}_a(t)|^2 \right) \tag{35}$$

is the partition function. We note that, by the mesh-free character of the shape functions (34), eq. (33) does not entail any ordering or connectivity between the monopoles and the method is line-free, as desired. In (34), the distance $1/\sqrt{\beta_a}$ sets the range of interaction for monopole a. Thus, only those monopoles that are at a distance of order $1/\sqrt{\beta_a}$ interact with monopole a, which renders the kinematic constraint (33) local.

3.2. Discretized force field

In order to discretize the rate functional (24), we begin by deriving the discrete configurational forces acting on the monopoles. To this end, we discretize the energy by inserting the monopole representation (27) into (8), with the result [3]

$$E^{\epsilon}(\{\boldsymbol{x}\}, \{\boldsymbol{\xi}\}) = \sum_{a=1}^{M} E_a^{\epsilon} + \sum_{a=1}^{M} \sum_{\substack{b=1 \\ b \neq a}}^{M} E_{ab}^{\epsilon}, \tag{36}$$

where we write $\{\boldsymbol{x}\} = \{\boldsymbol{x}_a\}_{a=1}^{M}$ and $\{\boldsymbol{\xi}\} = \{\boldsymbol{\xi}_a\}_{a=1}^{M}$ for short, and

$$
\begin{aligned}
E_{ab}^{\epsilon} = &-\frac{\mu}{4\pi} S^{\epsilon\epsilon}(\boldsymbol{x}_a, \boldsymbol{x}_b)(\boldsymbol{b}_a \times \boldsymbol{b}_b) \cdot (\boldsymbol{\xi}_a \times \boldsymbol{\xi}_b) + \\
&\frac{\mu}{8\pi} S^{\epsilon\epsilon}(\boldsymbol{x}_a, \boldsymbol{x}_b)(\boldsymbol{b}_a \cdot \boldsymbol{\xi}_a)(\boldsymbol{b}_b \cdot \boldsymbol{\xi}_b) + \\
&\frac{\mu}{8\pi(1-\nu)}(\boldsymbol{b}_a \times \boldsymbol{\xi}_a) \cdot \boldsymbol{T}^{\epsilon\epsilon}(\boldsymbol{x}_a, \boldsymbol{x}_b) \cdot (\boldsymbol{b}_b \times \boldsymbol{\xi}_b),
\end{aligned} \tag{37}
$$

5

is the interaction energy between monopoles a and b. In addition, the self-energy of the monopoles is obtained by taking the limit of $\boldsymbol{x}_b \to \boldsymbol{x}_a$, with the result

$$E_a^\epsilon = \frac{\mu}{8\pi} \frac{1}{2\epsilon} (\boldsymbol{b}_a \cdot \boldsymbol{\xi}_a)^2 + \frac{\mu}{8\pi(1-\nu)} \frac{1}{3\epsilon} |\boldsymbol{b}_a \times \boldsymbol{\xi}_a|^2. \quad (38)$$

We note that the self-energy of the monopoles is finite but diverges as $\epsilon \to 0$, as expected. The first (second) term in (38) is the energy of the *screw* (*edge*) component of the monopole. We see that screw monopoles $(\boldsymbol{b}_a \times \boldsymbol{\xi}_a = 0)$ are energetically preferable if $\nu > 1/3$ and edge monopoles $(\boldsymbol{b}_a \cdot \boldsymbol{\xi}_a = 0)$ are energetically preferable if $\nu < 1/3$.

The discrete configurational forces acting on the monopoles can now be computed directly from (36), by taking variations with respect to the monopole coordinates $\{\boldsymbol{x}\}$ while simultaneously taking the kinematic constraint (33) into account, with the result

$$\begin{aligned} \boldsymbol{f}_a^{\epsilon\epsilon} = \frac{\partial E^\epsilon}{\partial \boldsymbol{x}_a} &= \left(\frac{\partial E^\epsilon}{\partial \boldsymbol{x}_a}\right)_{\text{exp}} + \sum_{b=1}^M \frac{\partial E^\epsilon}{\partial \boldsymbol{\xi}_b} \frac{\partial \boldsymbol{\xi}_b}{\partial \boldsymbol{x}_a} \\ &= \left(\frac{\partial E^\epsilon}{\partial \boldsymbol{x}_a}\right)_{\text{exp}} + \sum_{b=1}^M \frac{\partial E^\epsilon}{\partial \boldsymbol{\xi}_b} \nabla N_a(\boldsymbol{x}_b) \cdot \boldsymbol{\xi}_b, \end{aligned} \quad (39)$$

where $(\partial E^\epsilon / \partial \boldsymbol{x}_a)_{\text{exp}}$ denotes the derivative of E^ϵ with respect to its explicit dependence on the monopole coordinates $\{\boldsymbol{x}\}$. We note that the elastic configurational forces $\boldsymbol{f}_a^{\epsilon\epsilon}$ on the monopoles comprise a direct term, corresponding to the direct dependence of E^ϵ on the monopole positions, and a geometrical term resulting from the dependence of E^ϵ on the monopole elements of line.

3.3. Discretized rate problem

Inserting the monopole *ansatz* into (24), we obtain the discrete rate functional

$$\begin{aligned} F^\epsilon(\{\boldsymbol{v}(t)\}; \{\boldsymbol{x}(t)\}) = \sum_{a=1}^M \psi(\boldsymbol{v}_a(t)) \, |\boldsymbol{\xi}_a(t)| \\ + \sum_{a=1}^M \left(f_a^{\epsilon\epsilon}(\{\boldsymbol{x}(t)\}) + f_a^{\text{ext}}(t)\right) \cdot \boldsymbol{v}_a(t). \end{aligned} \quad (40)$$

The corresponding Euler-Lagrange equations are

$$D\psi(\boldsymbol{v}_a(t))|\boldsymbol{\xi}_a(t)| + \boldsymbol{f}_a^{\epsilon\epsilon}(\{\boldsymbol{x}(t)\}) + \boldsymbol{f}_a^{\text{ext}}(t) = \boldsymbol{0}, \quad (41)$$

which, together with kinematic update (33) for the dislocation line elements, govern the motion of the monopoles.

In calculations, the macroscopic plastic strain rate induced by the motion of the dislocations is of interest. Such macroscopic plastic strain rate follows from a work argument as ([3])

$$\dot{\boldsymbol{\epsilon}}^p(t) = -\frac{1}{V} \sum_{a=1}^M \boldsymbol{b}_a(t) \odot (\boldsymbol{\xi}_a(t) \times \boldsymbol{v}_a(t)), \quad (42)$$

where $\odot$ denotes the symmetric dyadic product.

4. Numerical examples

We proceed to illustrate the range and scope of the line-free monopole method just outlined by means of a representative example, namely, the plastic hardening of nano-sized grains under monotonic loading. The grain-size dependence of strength is well-known to exhibit a reverse Hall-Petch effect, i.e. it decreases with decreasing grain size [9, 10, 11]. The majority of the experimental work on this area focuses on polycrystals with grain sizes up to 100 nm [12, 9].
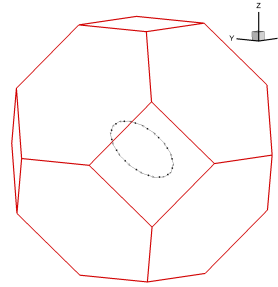
Figure 2: BCC grain containing a circular prismatic loop nucleated on the (0-11) plane and expanding under the action of an applied uniaxial stress (001).

We specifically consider the case of a single BCC grain embedded in an elastic matrix. The grain has

Table 1: Material properties for tungsten (W) (cf. [6]).

Lattice parameter (a)	0.317 nm
Burger's vector (b)	0.274 nm
Core size (ϵ)	0.548 nm
Nucleation radius (ρ_0)	1.233 nm
Shear modulus (μ)	16.0×10^{-8} N/nm^2
Poisson's ratio (ν)	0.278
CRSS (τ_0)	3.457×10^{-10} N/nm^2
Mobility (M)	1.456×10^{21} nm^2/Ns
GB stiffness (C)	1.02×10^{-10} N/nm^2
Critical time step (Δt_c)	6.756×10^{-12} s

the shape of a truncated octahedron and the grain boundary is assumed to be impenetrable to dislocations. The grain deforms by crystallographic slip in the class of $\{110\}\langle 111\rangle$ slip system under the action of a remotely applied uniaxial stress acting in the [001] direction.

We further focus on polycrystalline BCC tungsten with grain sizes in the range of 6-42 nm. The lattice parameter a, Burgers vector $b = (\sqrt{3}/2)\,a$, shear modulus μ and Poisson's ratio ν used in calculations are listed in Table 1. Atomistic simulation of dislocations in BCC transition metals [13, 14] further suggest a core size $\epsilon \sim 2b$ as a typical value.

We model nucleation by introducing small circular loops of radius ρ_0, commensurate with the annihilation radius of a loop, provided that the total energy of the system is decreased [3]. Given the small size of the grains considered, we assume that only one source is active per grain. For definiteness, we assume that the dislocation source is located on the plane $(0\bar{1}1)$ and at the center of the grain, Fig. 2. The loop radius at nucleation is taken to coincide with the annihilation radius of a circular loop, $\rho_0 = 2.25\,\epsilon$ [3]. The corresponding equilibrium resolved shear stress is [3]

$$\tau_0 = 0.07841 \times \frac{\mu b}{8\pi(1-\nu)\epsilon}, \qquad (43)$$

which evaluates to 3.457×10^{-10} N/nm^2, or $\sim 0.00216\mu$, in the ballpark of experimental observation in bcc transition metals [15, 16, 17].

Dislocation motion is assumed to be controlled by linear kinetics within the slip plane, with vanishing climb mobility. If we further assume phonon drag to be the rate-limiting mechanism, the mobility is $M = 1/B$, where B is the phonon drag coefficient. For W at 300K [18], $B^{\mathrm{edge}} \sim 6.87 \times 10^{-22}$ Ns/nm^2, whereas $B^{\mathrm{screw}} \sim 9.80 \times 10^{-22}$ Ns/nm^2. In calculations we take $B = B^{\mathrm{edge}}$, which gives a mobility $M = 1.456 \times 10^{21}$ nm^2/Ns.

We integrate in time the discretized governing equations (41) and (33) using an explicit two-stage Runge-Kutta method. In order to estimate the stable time step for explicit time integration, we consider an annihilating circular loop, in which range the Peach-Köhler force takes the form [3]

$$f = -\frac{\alpha\mu b^2 \rho}{8\pi(1-\nu)\epsilon^2}, \qquad (44)$$

with $\alpha \sim 4.613 \times 10^{-2}$. In this range, the mobility law becomes

$$\frac{d\rho}{dt} = -M\frac{\alpha\mu b^2 \rho}{8\pi(1-\nu)\epsilon^2} \equiv -\lambda\rho. \qquad (45)$$

Numerical stability then requires

$$\Delta t < \frac{1}{\lambda} = \frac{1}{M}\frac{8\pi(1-\nu)\epsilon^2}{\alpha\mu b^2} = \Delta t_c. \qquad (46)$$

Inserting the values of the parameters determined above, gives $\Delta t_c = 6.756 \times 10^{-12}$ s.

Finally, the impenetrability condition at the grain boundary is enforced by means of a potential that penalizes monopole excursions outside the grain. The restoring Peach-Köhler force is

$$f = -C\delta, \qquad (47)$$

where δ is the distance from the dislocation to the grain and C is a penalty stiffness [19]. Assuming the restoring force (47) to dominate, the mobility law becomes

$$\frac{d\delta}{dt} = -MC\delta. \qquad (48)$$

It follows from this analysis that numerical stability (46) is preserved if

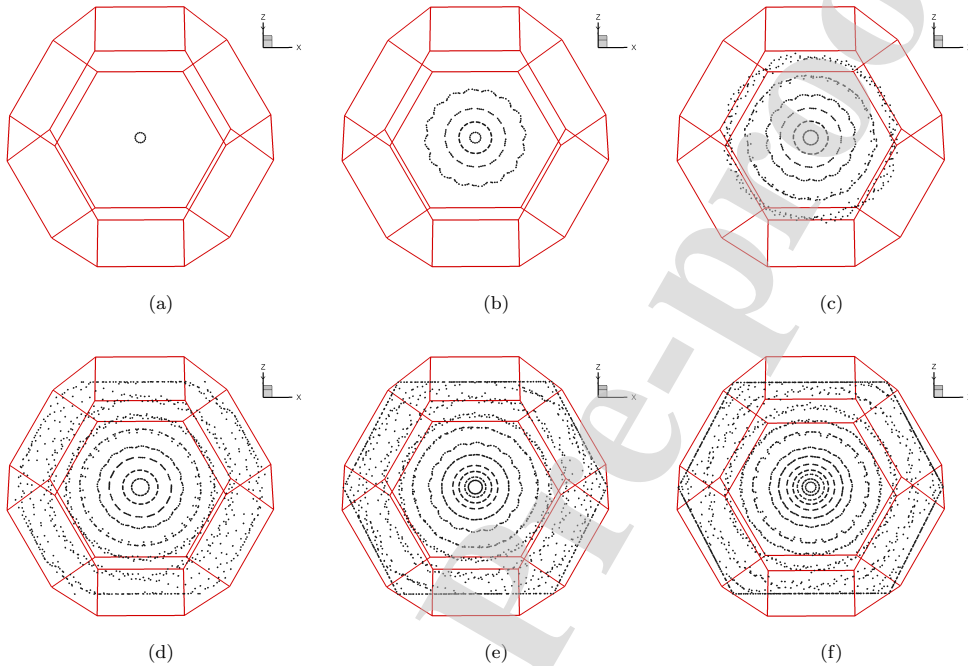$$C < \frac{1}{M\Delta t_c}. \qquad (49)$$

7

(a) (b) (c)

(d) (e) (f)

Figure 3: Evolution of dislocation activity in the 42 nm grain. (a) Initial configuration. (b) Strain 0.0005. (c) Strain 0.002. (d) Strain 0.005. (e) Strain 0.008. (f) Strain 0.01.

For the values of the parameters determined in the foregoing, we obtain $C < 1.02 \times 10^{-10}$ N/nm^2, which sets an upper bound on the stiffness that can be assigned to the grain boundary.

Fig. 3 shows the evolution of dislocation activity in the 42 nm grain. After nucleation, the new loop shields the source and its operation is shut off until the loop becomes sufficiently large. This transient shielding results in the intermittent emission of loops from the sources. Remarkably, as the loops grow their initial circular configuration loses stability and becomes wavy. The amplitude of the waviness increases with further growth until the lobes pinch-off, effectively doubling the loop. The calculations thus suggest that curvature-driven shape instabilities followed by pinch-off constitute a principal dislocation multiplication mechanism in nano-sized grains, where con-

finement effectively shuts off the operation of other conventional dislocation multiplication mechanisms such as double cross glide. As the dislocations reach the grain boundary, they arrest giving rise to a pile-up spanning the entire grain.

The confining effect of grain size on dislocation activity is shown in Fig. 4. The smallest-sized grain of size 6 nm can only fit one dislocation loop, which effectively shuts off further dislocation nucleation. As the grain size increases, the extent of dislocation nucleation and grow increases steadily, as does the complexity of the dislocation patterns at equilibrium. In particular, the pinch-off instability and dislocation multiplication mechanism is activated for grains larger than 24 nm and is suppressed in smaller grains

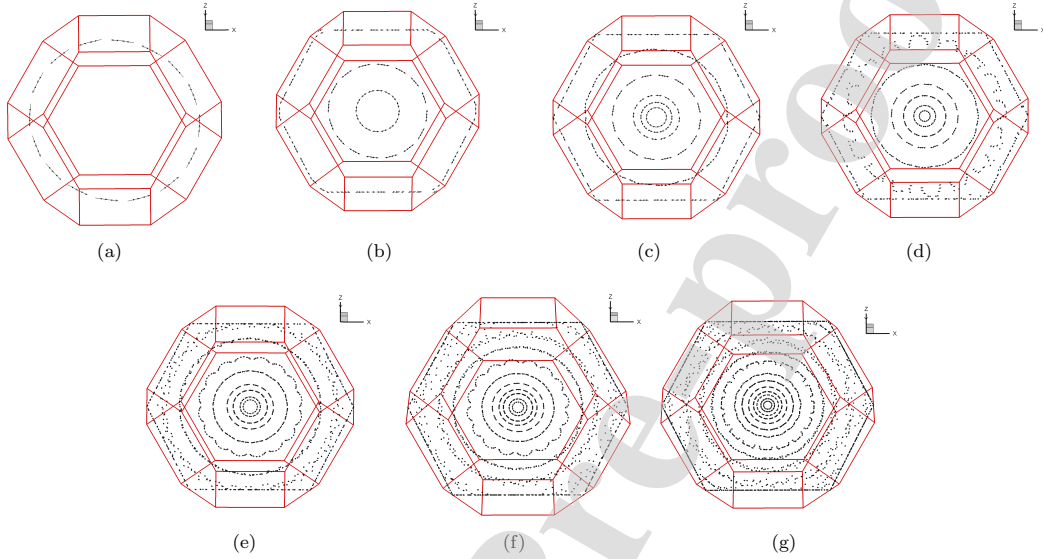Fig. 5 shows the computed stress-strain curves as a function of grain size. As the grain size increases,

8

Figure 4: Dislocation loop configurations in grains of different sizes at a strain of 1%. (a) 6 nm. (b) 12nm. (c) 18 nm. (d) 24 nm. (e) 30 nm. (f) 36 nm. (g) 42 nm.
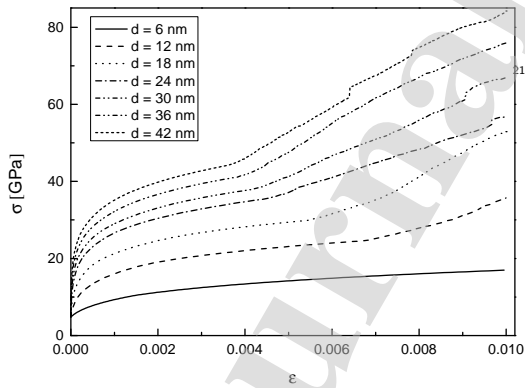

Figure 5: Computed stress-strain curves up to 1% strain for tungsten nano-grains ranging in size from 6 to 42 nm.

the number of dislocation loops that are nucleated also increases, as does the size of the dislocation pile-up. These trends result in a corresponding increase in the back-stress on the nucleation source, which in turn requires a comparatively higher level of applied stress for its operation.

The resulting dependence of the stress at an offset strain of 1%, taking as a measure of strength, on the grain size is further shown in Fig. 6. As may be seen, the dependence shows the reverse Hall-Petch effect characteristic of nano-sized grains [10]. A power-law fit of the form

$$\sigma = \sigma_0 + k\,d^a, \tag{50}$$

gives $\sigma_0 = -5.557 \times 10^{-8}$, $k = 4.040 \times 10^{-8}$ and $a = 0.329$. This exponent is in the ballpark of observation [20] and theoretical predictions [10].
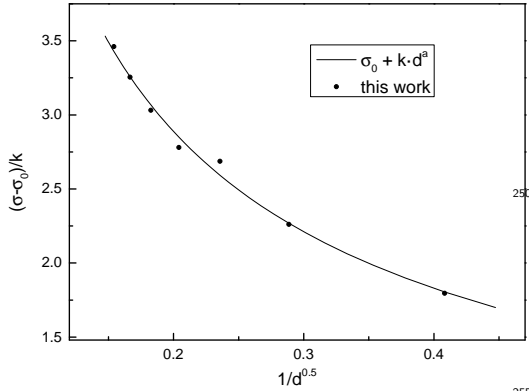
9

Figure 6: Computed strength (dots) as a function of the inverse square root of grain size in tungsten nano-grains. Power-law fit with $\sigma_0 = -5.557 \times 10^{-8}$, $k = 4.040 \times 10^{-8}$ and $a = 0.329$.

5. Concluding remarks

The monopole representation of dislocations is remarkable for its simplicity. The calculations have the structure of particle methods, where the 'particles', or monopoles, carry a Burgers vector and an element of line. The monopoles then interact through elastic interaction forces, which can be written down explicitly, and move according to a physical mobility law. In addition, a non-holonomic kinematical constraint, implemented through simple mesh-free interpolation, ensures that dislocation stretching and reorientation, together with the zero-divergence constraint of dislocation lines, are properly taken into account.

The ability of the monopole representation to track configurational and topological changes is also remarkable. Thus, the preceding calculations reveal a possibly new mechanism of dislocation multiplication operating at the nanoscale, resulting from curvature-driven loss of stability of the dislocation lines and subsequent pinch-off. The ability of the method to describe complex dislocation patterning and scaling relations is also noteworthy. In particular, the experimentally observed inverse Hall-Petch scaling arises naturally from the calculations as a result of a paucity of sources at the nanoscale ('source-starved nano-crystals') and the scaling of the backstresses induced by the equilibrium dislocation pileups.

References

[1] B. Li, F. Habbal, M. Ortiz, Optimal transportation meshfree approximation schemes for fluid and plastic flows, International Journal for Numerical Methods in Engineering 83 (12) (2010) 1541–1579.

[2] L. Fedeli, A. Pandolfi, M. Ortiz, Geometrically exact time-integration mesh-free schemes for advection-diffusion problems derived from optimal transportation theory and their connection with particle methods, International Journal for Numerical Methods in Engineering 112 (9) (2017) 1175–1193.

[3] A. Deffo, M. P. Ariza, M. Ortiz, A line-free method of monopoles for 3d dislocation dynamics, Journal of the Mechanics and Physics of Solids 122 (2019) 566 – 589.

[4] S. Conti, A. Garroni, M. Ortiz, The line-tension approximation as the dilute limit of linear-elastic dislocations, Archive for Rational Mechanics and Analysis 218 (2) (2015) 699–755.

[5] S. Conti, A. Garroni, A. Massaccesi, Modeling of dislocations and relaxation of functionals on 1-currents with discrete multiplicity, Calculus of Variations and Partial Differential Equations 54 (2) (2015) 1847–1874.

[6] J. P. Hirth, J. Lothe, Theory of Dislocations, McGraw-Hill, New York, 1968.

[7] T. Mura, Micromechanics of defects in solids, Kluwer Academic Publishers, Boston, 1987.

10

[8] M. Arroyo, M. Ortiz, Local maximum-entropy approximation schemes: a seamless bridge between finite elements and meshfree methods, International Journal for Numerical Methods in Engineering 65 (13) (2006) 2167–2202.

[9] Z. C. Cordero, B. E. Knight, C. A. Schuh, Six decades of the hall–petch effect – a survey of grain-size strengthening studies on pure metals, International Materials Reviews 61 (8) (2016) 495–512.

[10] R. Masumura, P. Hazzledine, C. Pande, Yield stress of fine grained materials, Acta Materialia 46 (13) (1998) 4527 – 4534.

[11] C. Pande, K. Cooper, Nanomechanics of hall–petch relationship in nanocrystalline materials, Progress in Materials Science 54 (6) (2009) 689 – 706.

[12] U. K. Vashi, R. W. Armstrong, G. E. Zima, The hardness and grain size of consolidated fine tungsten powder, Metallurgical Transactions 1 (6) (1970) 1769–1771.

[13] W. Xu, J. A. Moriarty, Atomistic simulation of ideal shear strength, point defects, and screw dislocations in bcc transition metals: Mo as a prototype, Physical Review B 54 (10) (1996) 6941–6951.

[14] L. H. Yang, P. Söderlind, J. A. Moriarty, Accurate atomistic simulation of $(a/2)\langle 111 \rangle$ screw dislocations and other defects in bcc tantalum, Philosophical Magazine 81 (5) (2001) 1355–1385.

[15] L. Hollang, M. Hommel, A. Seeger, The flow stress of ultra-high-purity molybdenum single crystals, Physics Status Solidi A 160 (1997) 329–354.

[16] T. Suzuki, Y. Kamimura, H. O. K. Kichner, Plastic homology of bcc metals, Philosophical Magazine A 79 (7) (1999) 1629–1642.

[17] A. Seeger, L. Hollang, The flow-stress asymmetry of ultra-pure molybdenum single crystals, Materials Transactions, JIM 41 (1) (2000) 141–151.

[18] G. Po, Y. Cui, D. Rivera, D. Cereceda, T. D. Swinburne, J. Marian, N. Ghoniem, A phenomenological dislocation mobility law for bcc metals, Acta Materialia 119 (2016) 123 – 135.

[19] S. Conti, M. Ortiz, Dislocation microstructures and the effective behavior of single crystals, Archive for Rational Mechanics and Analysis 176 (2005) 103–147.

[20] V. Gertsman, M. Hoffmann, H. Gleiter, R. Birringer, The study of grain size dependence of yield stress of copper for a wide grain size range, Acta Metallurgica et Materialia 42 (1994) 3539–3544.

11

Conflict of Interest

Declaration of interests

☒ The authors declare that they have no known competing financial interests or personal relationships that could have appeared to influence the work reported in this paper.

☐The authors declare the following financial interests/personal relationships which may be considered as potential competing interests: